







RESEARCH ARTICLE

Design and fabrication of anisotropic SiO₂ gyroid bioscaffolds with tunable properties

Ka-Wai Yeung¹, Chi-Yeung Mang¹, Quan-Jing Mei², Chi Ho Wong³,
Chak-Yin Tang^{1,4*}, Xin Zhao², Wing-Cheung Law¹, Gary Chi-Pong Tsui¹,
and Zhenjia Huang¹

¹Department of Industrial and Systems Engineering, Faculty of Engineering, The Hong Kong Polytechnic University, Hong Kong, China

²Department of Applied Biology and Chemical Technology, Faculty of Science, The Hong Kong Polytechnic University, Hong Kong, China

³Department of Physics, School of Science, The Hong Kong University of Science and Technology, Hong Kong, China

⁴State Key Laboratory of Ultra-precision Machining Technology, Department of Industrial and Systems Engineering, Faculty of Engineering, The Hong Kong Polytechnic University, Hong Kong, China

Abstract

This paper introduces a mathematical approach and additive manufacturing process to customize the mechanical properties of sheet gyroid bioscaffolds and mimicking the intricate architecture of natural bone. By defining the parameters of the level-set equation, scaffolds with spatially controlled porosity and anisotropic properties can be fabricated through digital light processing and microwave heating. A new susceptor-assisted hybrid pyrolysis-sintering process was developed, resulting in a significant enhancement in quality and mechanical properties of the three-dimensional (3D)-printed ceramic compared to conventional methods. The enhancements are originated from the improved densification, accelerated sintering kinetics, promotion of cristobalite phase transformation, and reduced defect volume under microwave heating. Sheet gyroid scaffolds with radially graded porosity and anisotropic properties were fabricated. Despite the porosity distribution, an increase in the unit cell's aspect ratio amplified the anisotropic mechanical properties. This was also accompanied by a slight decrease in cell proliferation efficiency possibly due to variations in Gaussian curvatures.

***Corresponding authors:**

Chak-Yin Tang
(cy.tang@polyu.edu.hk)

Citation: Yeung K-W, Mang C-Y, Mei Q-J, et al. Design and fabrication of anisotropic SiO₂ gyroid bioscaffolds with tunable properties. *Int J Bioprint*. 2024;10(5):3609. doi: 10.36922/ijb.3609

Received: May 8, 2024

Accepted: June 11, 2024

Published Online: August 8, 2024

Copyright: © 2024 Author(s). This is an Open Access article distributed under the terms of the Creative Commons Attribution License, permitting distribution, and reproduction in any medium, provided the original work is properly cited.

Publisher's Note: AccScience Publishing remains neutral with regard to jurisdictional claims in published maps and institutional affiliations.

Keywords: Biomimetic structure; Triply periodic minimal surface; Microwave technology; 3D Printing; Ceramic bioscaffold

1. Introduction

Ceramic bioscaffolds that mimic the physical and mechanical properties of natural human bone are crucial to achieve optimal bone regeneration. Achieving this involves precise manipulation of factors like volume fraction, pore size, and surface topography. Triply periodic minimal surfaces (TPMS), particularly the gyroid structure, offer promising scaffold design for bone regeneration.¹⁻⁴ Their geometries can be meticulously controlled through

mathematical algorithms.⁵ The equation-driven architecture enables customization of lattice type, unit cell dimensions, strut sizes, volume fraction, and curvature distribution,⁶ which is conducive to regulating cellular behaviors.⁷ Recent studies have demonstrated that mimicking the anisotropy of natural bone, along with spatially controllable porosity, can achieve tunable mechanical properties and reduce the *in vivo* stress shielding effect, potentially improving scaffold integration.⁸ This allows for the optimization of mechanical properties, enabling the creation of scaffolds that are strong and stiff where needed, yet lightweight and porous in other regions. This tunability in mechanical properties is crucial for matching the mechanical behavior of the scaffold to the surrounding bone tissue, and consequently enhances the integration with the host bone, promoting more effective bone repair and regeneration. Leveraging advanced additive manufacturing techniques and innovative 3D-printable biomaterials are expected to contribute to the development of functional biodevices.^{7,9–11} However, optimal TPMS design for enhanced bone regeneration remains a topic of ongoing research.

Three dimensional (3D) printing is a promising technology for producing bone implants and constructs due to the capability of fabricating complex, precise, and customized structures with controlled architectures and properties.¹² The major advantages of 3D cell culture are the ability to create a realistic microenvironment for cells, facilitate cell–cell and cell–matrix interactions, thus enhancing the cell growth and proliferation.^{13,14} Currently, 3D printing of ceramic can be achieved by developing photocurable ceramic/polymer composites followed by lithography-based process such as stereolithography and digital light processing (DLP).^{15–18} However, generation of dense 3D ceramic generally required lengthy debinding and sintering processes to achieve highly densified products, which reduce the throughput of the manufacturing process and limit their potential applications. To mitigate this limitation, susceptor-assisted microwave heating (SMWH) offers a promising and time-saving alternative for sintering ceramic specimens, due to its intrinsic heating mechanism that lowers sintering activation energy and processing temperature.^{19–21} Despite offering a more reliable and controllable sintering process,^{22,23} challenges such as crack formation associated with the rapid heating have limited its utilization in additive manufacturing processes.²⁴ Further research is needed to improve the process and fully exploit the advantages of microwave (MW) technology to enhance the throughput of the 3D scaffolds manufacturing.

In this proof-of-concept study, we introduced a design methodology for creating sheet gyroid structures with tailored geometrical properties, employing bioinert silica as the model materials due to its superior mechanical

properties and stability compared to other bioceramics. By controlling the parameters of the level-set equations of the gyroid structure, we achieved spatially controlled porosity and anisotropic properties, generating structures with radially graded porosity (40–60%) to mimic trabecular bone. The scaffolds were fabricated through DLP, followed by a susceptor-assisted hybrid pyrolysis-sintering (SHPS) process utilizing MW heating. This innovative method effectively reduces defects and mitigates crack formation during rapid MW sintering, leading to reduced defect volume by 16.81% and improved compressive strength by 336% compared to conventional furnace heating. Additionally, our study revealed that an increase in aspect ratio of the unit cell amplified the anisotropic mechanical properties of the gyroid structure. However, while the scaffolds exhibit minimal cytotoxicity, this adjustment slightly decreases cell proliferation efficiency compared to the uniform gyroid structure due to variations in Gaussian curvatures. This paper presents a design approach for fabricating equation-driven TPMS structures, including but not limited to gyroid structures, with controlled mechanical properties, and elucidates the correlation between geometric characteristics and both mechanical properties and *in vitro* cell responses. In addition to the potential of mitigating the stress shielding effect through computer-aided scaffold design, our findings also have wider implications for advanced biodevice development. This encompasses the integration of piezoelectric materials,²⁵ enabling advanced functionalities such as directional biosensing capabilities.

2. Methodology

This study presents a mathematical approach and additive manufacturing process for fabricating different gyroid scaffolds with precisely controlled geometrical properties. Gyroid scaffolds with controlled porosity and tunable anisotropic characteristics were achieved by manipulating the double iso-surface value and the geometric parameters of the level-set equation. DLP technology was utilized to realize the gyroid design, and an innovative pyrolysis-sintering hybridization method based on SMWH was implemented with the goal of improving the quality of the final product. Through this integrated approach, we aimed to demonstrate an advanced design and fabrication strategy of scaffolds for bone regenerative engineering, facilitating their broader application across various fields.

2.1. Design of graded gyroid structure with controlled properties

Different criteria need to be considered when designing a scaffold for bone tissue engineering to achieve optimal physical, mechanical, and morphological properties. Sheet gyroid-type TPMS structure was adopted due to its excellent interconnectivity, fluid permeability, and

mechanical properties.²⁶ The geometrical properties of the structure can be manipulated by controlling the parameters of the level-set equations of the structure, which are a combination of trigonometric functions that satisfy the equation $\varphi(x, y, z) = c$. The sheet gyroids can be described by the following level-set equation:

$$\begin{aligned} &\sin(2\alpha\pi x) \cos(2\beta\pi y) + \sin(2\beta\pi y) \\ &\cos(2\gamma\pi z) + \sin(2\gamma\pi z) \cos(2\alpha\pi x) = c \end{aligned} \quad (\text{I})$$

where the geometric parameters α , β , and γ control the unit cell dimensions in the x , y , and z directions, respectively; c is a function that defines the iso-surface of the sheet gyroid structure which controls the thickness of the sheet and therefore affects the solid volume fraction (ϕ) of the structure. To create a solid domain, a double iso-surface can be defined by solving $-c \leq \varphi_{gy} \leq c$. Scaffold with interconnected pores is desirable to mimic the biological bone tissue, as it promotes nutrient diffusion, and facilitates cell attachment, differentiation, and colonization.³ Studies have shown that TPMS scaffolds with 30–60% porosity exhibit reduced stress shielding effect.²⁷ Therefore, the parameters α , β , and γ were fixed at 0.50, and the value of c ranging from 0.62 to 0.91 was identified to achieve desired ϕ (40–60%) of the gyroid structure. Figure 1 illustrates the $8 \times 8 \times 8 \text{ mm}^3$ sheet gyroid structures with different value of ϕ , including 40% (40VF-gy), 50% (50VF-gy), 60% (60VF-gy), and their corresponding c values.

Graded gyroid scaffold that mimics the anisotropic structure of natural bone can be beneficial for mitigating stress shielding effect and promoting cell growth. Graded porosity and structural anisotropy were achieved by adjusting the parameters of the level-set equation (Equation (I)), specifically by defining the parameters for the unit cell dimension and a function for the iso-value $c = C(x, y, z)$. Gyroid structures with varying aspect ratios of the unit cell were constructed by controlling the parameter γ (Figure 2a). It is noteworthy that the value of ϕ in the sheet gyroid structure remained independent of the γ value but showed a positive correlation with the c value (Figure 2b). A radially graded porosity within the gyroid scaffold was achieved by assigning a control function to $C(x, y, z)$ as follows:

$$C(x, y, z) = a(x^2 + y^2 + z^2) + b \quad (\text{II})$$

To mimic the pore distribution of natural bone, which has a denser outer part (cortical bone) and a more porous inner part (cancellous bone), the center porosity of the gyroid structure is set to 60% ($C_{\phi=60\%} = 0.91$) and the outer porosity to 40% ($C_{\phi=40\%} = 0.62$), the coefficients value can be obtained as follows:

$$\begin{cases} C_{x=y=z=0} = C_{\phi=60\%} = 0.91 \\ C_{x=y=z=d/2} = C_{\phi=40\%} = 0.62 \end{cases} \quad (\text{III})$$

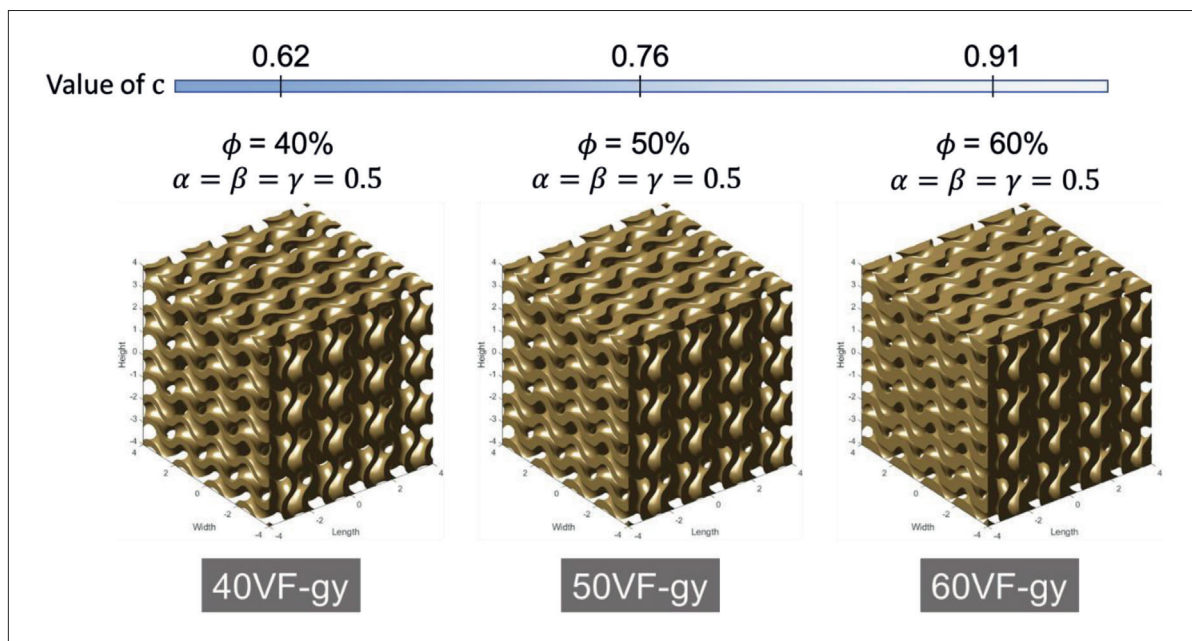


Figure 1. 3D models for the gyroid structure with different volume fractions ϕ : 40VF-gy ($\phi = 40\%$, $c = 0.62$), 50VF-gy ($\phi = 50\%$, $c = 0.76$), and 60VF-gy ($\phi = 60\%$, $c = 0.91$).

From **Equations (II)** and **(III)**, the following equation can be obtained:

$$C(x, y, z) = 0.02(x^2 + y^2 + z^2) + 0.62 \quad (\text{IV})$$

where d represents the width or diameter of the structure. **Figure 2c** illustrates the graded sheet gyroid scaffolds with different γ value (γ .25-FGgy, γ .33-FGgy, and γ .50-FGgy) and the corresponding porosity distribution within the scaffold. Computer-aided design (CAD) models for the gyroid structures, including 40VF-gy, 50VF-gy, 60VF-gy, 57.55VF-gy, γ .25-FGgy, γ .33-FGgy, and γ .50-FGgy (**Figure 2c**), were generated using MSLattice.⁵ **Table 1** summarizes the total surface area, ϕ , and porosity of all gyroid structure. Besides ϕ , the total surface area of the structure is also affected by the γ and $C(x, y, z)$ values. For the graded gyroid structures,

although the values of ϕ are identical due to the same $C(x, y, z)$ control function, the change in γ value can effectively tune the total surface area. This feature enables precise adjustment of the geometric properties of the cellular structure, offering a wide range of potential configurations.

2.2. Preparation of 3D-printed green specimens

The 3D printing was performed on a DLP printer (Admaflex 130, the Netherlands). The 3D printing process employed a commercial photosensitive silicon dioxide (SiO_2) slurry (AdmaPrint S130, the Netherlands), which had a high ceramic loading exceeding 75 wt.% as confirmed by the thermogravimetric analysis (TGA) (**Figure 3a**). CAD models of the sheet gyroid structures in STL format were imported into the built-in software and sliced for the printing process. The layer thickness of 60 μm was set with an exposure intensity and time of 60 mW/cm² and 2000 ms, respectively. After printing, the structures underwent

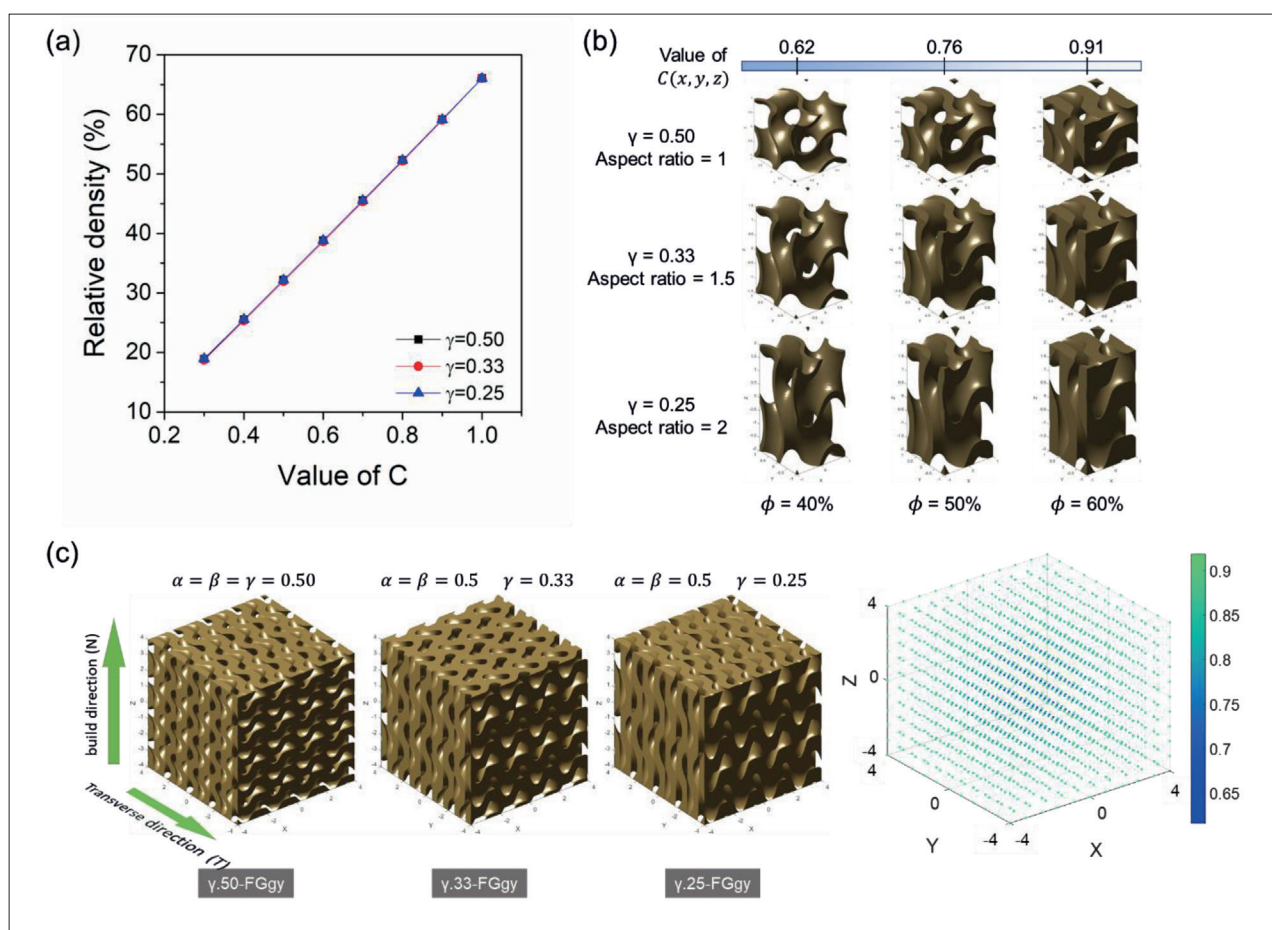


Figure 2. Parametric influence on SiO_2 gyroid scaffolds. (a) The effect of parameters on the volume fraction ϕ . (b) 3D unit cell model at different parameters. (c) Illustration of different radial graded gyroid structures (the building direction [B] of the DLP technology and the transverse direction [T] are also shown) and $C(x, y, z)$ value distribution within the structure (right figure).

Table 1. Summary of the geometric properties of the different sheet gyroid structures.

Model	α	β	γ	Value of $C(x, y, z)$	Total surface area (mm^2)	ϕ (%)	Designed porosity (%)
40VF-gy	0.50	0.50	0.50	0.62	1602.8	40	60
50VF-gy				0.76	1567.3	50	50
60VF-gy				0.91	1512.5	60	40
57.55VF-gy	0.50	0.50	0.50	0.88	1525.2	57.55	42.45
γ .50-FGgy	0.50	0.50	0.50	$C(x, y, z)$	1551.9	57.55	42.45
γ .33-FGgy			0.33		1424.5	57.55	42.45
γ .25-FGgy			0.25		1363.8	57.55	42.45

development using isopropyl alcohol under ultrasonication for 30 min to remove excess slurry, followed by overnight drying in a vacuum chamber at 60°C.

2.3. Post-processing of the DLP-printed structures

This study first employed a conventional furnace (Nabertherm HT29/17, Germany) and a commercial single-mode 2.45 GHz MW furnace (HAMiLab-HV3000, Synotherm, China) for the debinding and sintering process of DLP 3D-printed specimens. A comparative study was performed to assess the effectiveness of the SMWH process for the post-processing of 3D-printed cube specimens. For SMWH process, a kiln with 2-mm-thick inner layer of silicon carbide (SiC) was used as the susceptor for assisting the MW heating. The temperature profile of the debinding was defined by the TGA of the photo-cured SiO_2 slurry, as shown in Figure 3a and b. From the TGA and derivative thermogravimetric (DTG) curves within the temperature range of 50–800°C, weight loss started to occur at above 325°C and a maximum weight loss was recorded at 425.82°C. The weight loss rate reduced at around 525°C, signifying the decomposition of most organic matter. Within the test temperature, a maximum weight loss of 21.56% was recorded.

According to the TGA result, the debinding and sintering profile for the 3D-printed specimens was established. A fast-heating rate of 20°C/min was applied throughout the study to exploit the merits of MW heating, unless otherwise specified. The same heating profile, involving a two-step heating as depicted in Figure 3b, was used for both SMWH and conventional furnace heating process under air atmosphere. In brief, the specimens underwent a 30-min dwell time at 600°C for debinding, followed by sintering at 1150°C for a desired dwell time. Subsequently, the specimens were allowed to cool down at

a rate of 1.5°C/min to room temperature. Different dwell times of 10, 20, 40, 80, 120, and 180 min were selected to compare the efficacy of the SMWH process (specimens denoted as MW10m, MW20m, MW40m, MW80m, MW120m, MW180m) and conventional furnace heating (specimens denoted as CS40m, CS80m, CS120m, CS180m). The density, mechanical properties, and the structural properties of the sintered specimens were studied and compared.

Subsequently, an innovative SHPS process was employed using the MW furnace aimed at enhancing the properties of the sintered specimens (Figure 3c). This involves the following stages:

1. In the first stage, the 3D-printed green specimens were heated to 600°C with a dwell time of 30 min under nitrogen (N_2) atmosphere. Then, the specimens were cooled at a rate of 1.5°C/min to room temperature. During this stage, pyrolysis instead of debinding of the green specimens occurred, leaving residual carbon after the first heating stage and retaining the geometrical features of the 3D-printed specimens.²⁸
2. In the second stage, a two-step sintering process under air atmosphere was employed, where the specimens were dwell at 800°C for 10 min to completely remove the residual carbon, followed by a dwell at 1150°C for 120 min. The specimens were allowed to cool down at a rate of 1.5°C/min to room temperature.

The quality of the specimens produced using the SHPS process (specimens denoted as SHPS120m) was compared with those fabricated using conventional furnace, which followed the manufacturer recommended heating profile with the same sintering dwell time of 120 min (specimens denoted as RCS120m), as shown in Figure 3d.

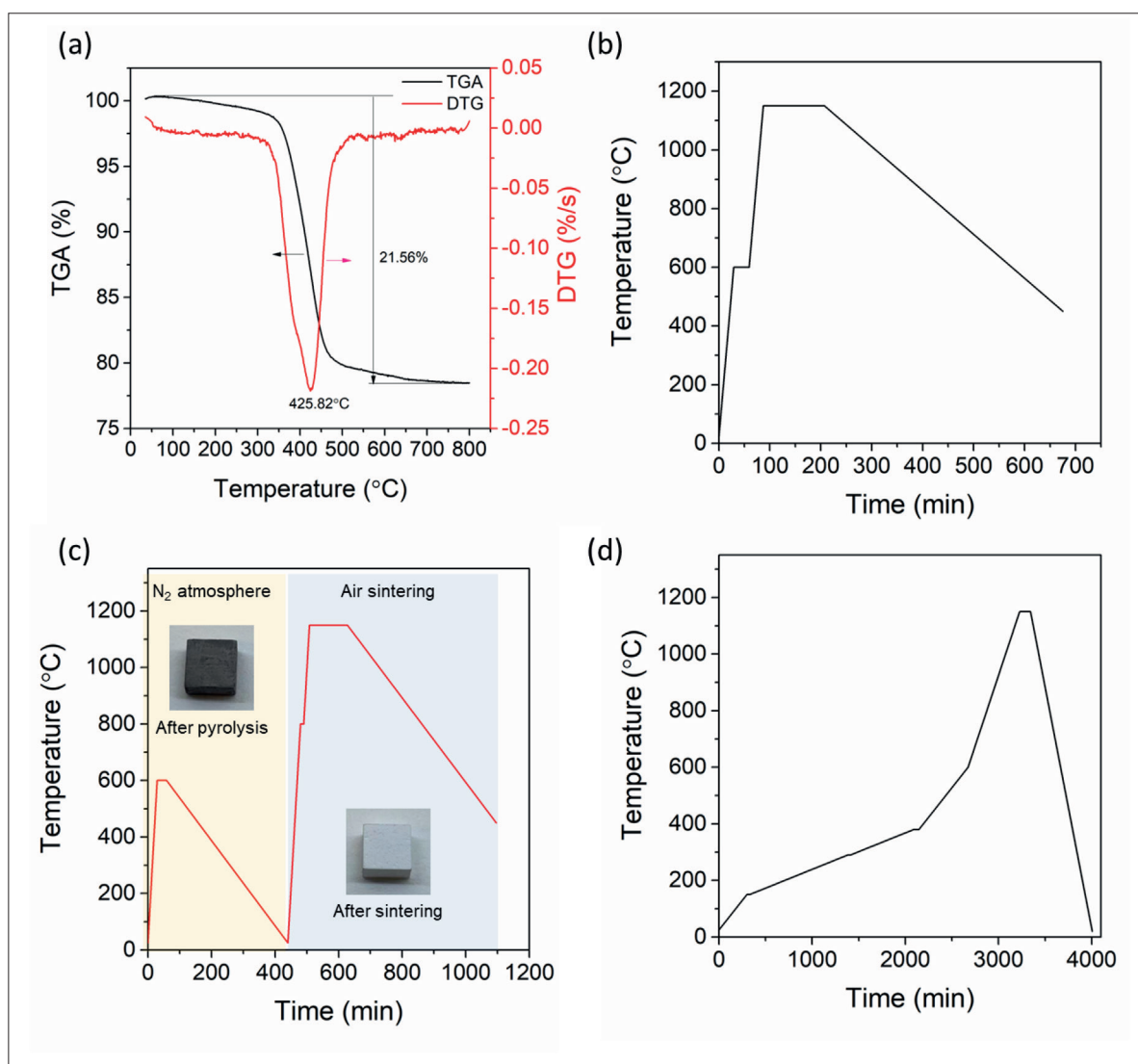


Figure 3. Thermal analysis and heating profiles of 3D printed specimens. (a) Thermogravimetric analysis (TGA) and derivative thermogravimetric (DTG) curves of cured S130 photoresin. (b) The heating profile for the susceptor-assisted microwave heating (SMWH) process under air atmosphere. (c) The susceptor-assisted hybrid pyrolysis-sintering (SHPS) heating profile for debinding and sintering. (d) The heating profile as recommended by the manufacturer using conventional furnace (copyright permission from Admatec).

2.4. Characterization methods

The morphology of the 3D-printed green specimens and sintered specimens were observed using a scanning electron microscope (SEM; TESCAN VEGA3) to assess the presence of defects or cracks after DLP 3D printing and the post-thermal processing. The lateral face corresponding to the printing direction was observed. The bulk density measurement of the sintered cube specimens was conducted using Archimedes' principle by means of a custom-made setup on a balance (Kern ADJ 200-4, Germany) using the theoretical density of 2.2 g/cm³ of amorphous SiO₂.²⁹ The porosity of the 3D-printed

green specimens and sintered specimens was analyzed by micro-computed tomography (μ -CT; YXLON FF35 CT, Germany), and the defects were captured. All specimens were subjected to a source voltage and current within the ranges of 70–80 kV and 100–110 μ A, respectively. The Y.FXT 190.61 transmission tube, which has a 2D detail detectability of 150 nm, was used. X-ray radiographs of the specimens were recorded at various angles, and the projection images were then reconstructed and analyzed using the VGStudio Max 3.5 software. The phase composition of the specimens sintered under varying conditions was characterized using an X-ray

diffractometer (XRD; SmartLab 9 kW). The specimens were subjected to CuK α radiation ($\lambda = 1.54059 \text{ \AA}$) in the 2-theta range of 10° – 80° , with a scanning rate of $10^\circ/\text{min}$, and operated at 45 kV and 200 mA.

The compressive properties of the sintered ceramic specimens were evaluated by uniaxial compression tests using (INSTRON 68TM-50, USA). For each set of 3D-printed ceramic specimens, including both cube and gyroid structures, three samples were tested, and the average results were recorded. For the cube samples, the load was applied along the build direction during 3D printing to evaluate the mechanical properties enhanced by the SHPS process. To evaluate the anisotropic properties of the graded gyroid structures, compression tests were performed along both the build (N) and transverse (T) directions (Figure 2c). The peak compressive strength before failure and the stress–strain behavior were recorded. The tests were carried out at a crosshead speed of 0.5 mm/min until the specimen failed, following the ASTM C1424 standard.

2.5. *In vitro* cell culture experiment

Bone marrow-derived mesenchymal stem cells (BMSCs; Cyagen, Hong Kong) were used to examine the cytocompatibility of the graded gyroid scaffolds, including γ .50-FGgy, γ .33-FGgy, and γ .25-FGgy, with $\phi = 57.55\%$. The cell culture medium was prepared by α -MEM supplemented with 10% fetal bovine serum and 1% penicillin/streptomycin. The scaffolds were disinfected using an autoclave and then washed with phosphate-buffered saline (PBS). The cytocompatibility of the scaffolds was evaluated by seeding BMSCs onto the scaffolds. After putting different scaffolds in the bottom of a 24 well-plate, 1 mL BMSC suspension (2×10^4 cells/mL) was added onto the scaffolds and pipetted for three times to ensure the cell suspension can permeate into the scaffolds. All samples were cultured at 37°C in an incubator with 5% CO_2 . After 6 h of cell seeding, the well-plates were changed to remove the unattached cells on the scaffolds. After 1, 3, and 7 days of incubation, the cell viability was assessed by Live/Dead kit according to the manufacturer's protocol. The quantification of cell viability was determined by the ratio of the viable cells to all cells in eight randomly selected images. In addition, the cell number on scaffolds at different time points was evaluated by dissociating the cells with trypsin-EDTA solution and counted by the hemocytometer. The cell density was calculated through normalizing the cell number by the surface area of the scaffolds. To investigate the effects of the graded structure on cell proliferation, a uniform gyroid structure with the same value of ϕ , i.e., 57.55% (57.55VF-gy), was also used for comparison.

3. Result

3.1. Comparative study of the SMWH and conventional post-thermal processing

3.1.1. Effect of processing conditions on physical properties of the sintered ceramic

The efficacy of SMWH process was studied through studying the properties of 3D-printed and sintered ceramic cube. The effects of sintering dwell times under the SMWH process and conventional debinding and sintering were investigated. Figure 4a presents the XRD spectra of the ceramic cube specimens fabricated under different processing conditions. For all specimens prepared through the conventional sintering (CS), a broad peak at 21.3° was detected, corresponding to the amorphous structure of the SiO_2 . A low peak intensity was observed at 21.8° for CS120m, indicating the formation of cristobalite phase under a prolonged dwell time. In contrast, almost all specimens fabricated through the SMWH process show predominate peaks for cristobalite at 21.8° and 36.1° . For MW120m, the intensity of the peaks increased significantly. More amorphous SiO_2 transformed into crystal structure when the dwell time increased. In comparison with the CS process, the SMWH process facilitates rapid and efficient energy transfer due to the intrinsic features of MW heating, which also result in reduced activation energy for nucleation and enhanced crystallization during the sintering process.²⁰

The physical properties of the sintered ceramic cube under different processing conditions were characterized in terms of their percentage shrinkage, relative density, and the major crystalline structure. Figure 4b depicts shrinkage in the length (L), width (W), and height (H) of the specimens. As the dwell time increased, all specimens exhibited an increase in shrinkage across all dimensions (L , W , and H). For the SMWH process, the shrinkage percentage of the specimens sharply increased from dwell time of 10 to 80 min, while the increase become less obvious when the dwell time further extended to 180 min. The highest shrinkage percentages were recorded as 7.58%, 7.67%, and 8.25% in the L , W , and H dimensions, respectively. Similarly, the specimens prepared through the CS process demonstrated similar trend of the shrinkage percentage as the dwell time increases, but with considerably lower shrinkage percentage compared to the SMWH process. While all specimens fabricated through CS process shrank almost isotropically, a higher percentage of shrinkage in H compared to W and L was recorded for the specimens prepared through the SMWH process. This is because during the layer-by-layer printing process, the sedimentation of ceramic powder creates a resin-rich region on top of each printing layer, forming a lamellar

structure in the 3D-printed specimens after curing.³⁰ The lamellar structure generally disappears after the post-thermal treatment and formed dense ceramic parts. As a result, after the debinding and sintering process, the 3D-printed structures experience larger shrinkage in the H dimension. However, this phenomenon was not observed in the specimens prepared through the CS process. This is likely due to the incomplete debinding due to the high heating rate, which adversely affects the densification of the specimens.

The relative density of the specimens was also compared, as shown in Figure 4c. When subjected to the same heating profile, the specimens fabricated through the SMWH process exhibited higher relative densities compared to those from the CS process. The relative density of the MW specimens ranged from 95.38% to 97.4%, while the CS specimens showed values ranging from 91.89% to 93.49%. These findings suggest that the SMWH process plays a significant role in promoting

densification and the formation of a crystal structure in the ceramic cube specimens. The SMWH process promotes formation of cristobalite crystal structure in the ceramic cube specimen and facilitates densification, reducing the energy barrier for sintering compared to conventional furnace heating.²² As a result, density of the specimens closely approximates to the theoretical density value of 2.2 g/cm³ for amorphous SiO₂ due to the higher theoretical density value of the cristobalite structure in SiO₂ than the amorphous form. On the other hand, specimens prepared through conventional heating exhibit lower relative density, primarily due to the fast heating rate and short sintering time employed. These conditions may lead to the incomplete removal of the organic binders before reaching the sintering temperature. As a result, the SiO₂ particles are loosely in contact with each other, impeding the diffusion process during sintering. The SMWH process shows a promising result in achieving higher relative density compared to the conventional furnace heating, indicating

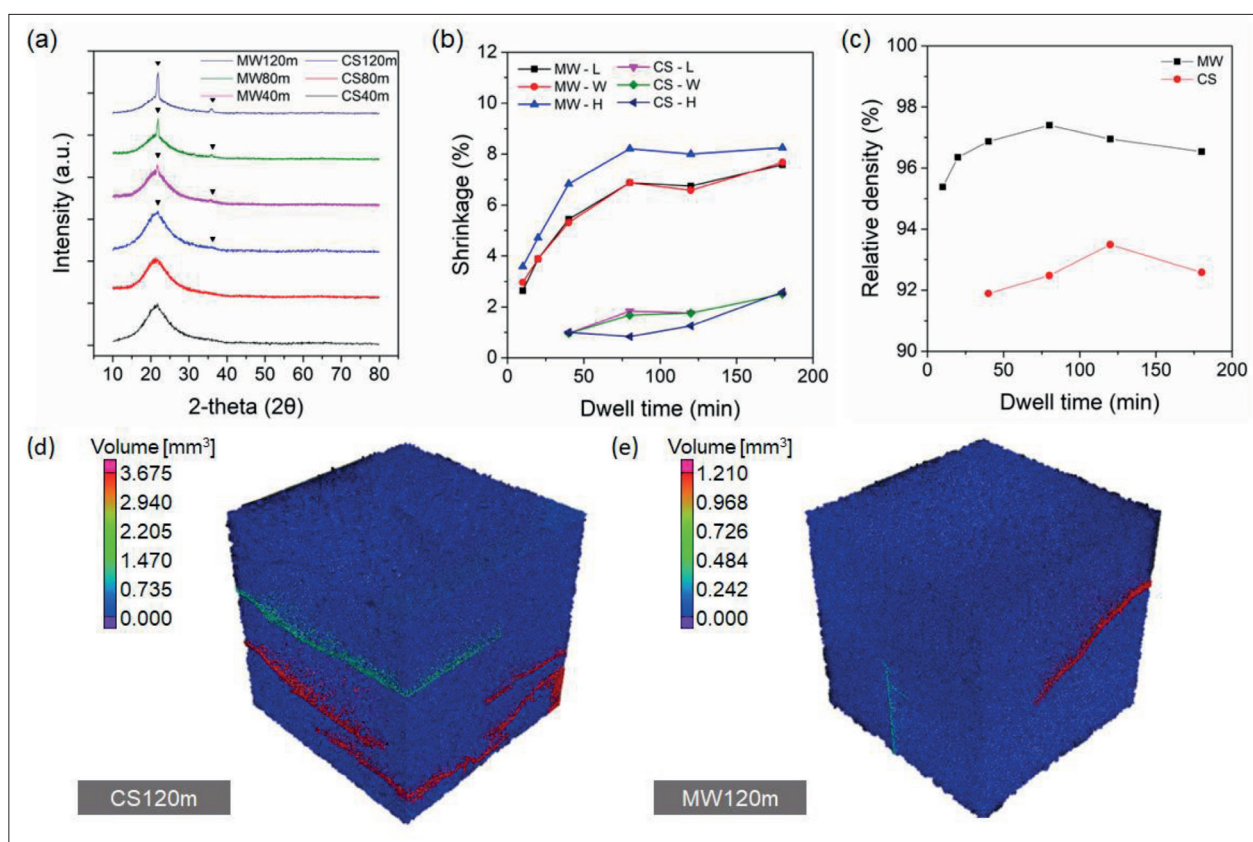


Figure 4. Comparative analysis of 3D-printed ceramic cubes. (a) X-ray diffraction (XRD) pattern for the 3D-printed ceramic cube specimens. (b) Dimensional shrinkage for the ceramic cube specimens processed through susceptor-assisted microwave heating (SMWH) and conventional furnace heating. L , W , and H correspond to the length, width, and height of the specimens, respectively. (c) The effect of the dwell time of sintering on the relative density of the specimens with respect to the theoretical density of amorphous SiO₂. The 3D reconstructed image obtained through micro-computed tomography (μ -CT) showing the defect distribution in the (d) CS120m and (e) MW120m specimens.

its potential as a post-processing technique for 3D-printed green parts to produce denser and more structurally robust ceramic materials.

Figure 4d and e presents the 3D reconstructed image obtained through μ -CT showing the defect distribution in the CS120m and MW120m specimens, respectively. Abundant cracks were formed, and larger defect volumes were observed in the CS120m specimens after sintering compared to MW120m. Under conventional heating, the fast heating rate leads to uneven heating, creating thermal stress, and thus promote crack formation during the heating process.³¹ Cracks were also observed for the MW120m specimens, despite their smaller defect volume. This can be attributed to the rapid generation of gas from the decomposition of the binder during the debinding stage, leading to the formation of larger voids within the specimens and making them prone to crack formation. Besides, the cracks were found on the lamellar facets. Owing to the layer-by-layer formation mechanism inherent to the DLP technology, weak points were created that are susceptible to crack initiation and propagation.³⁰ Despite the advantages offered by the SMWH process, the formation of cracks may have a detrimental effect on the mechanical properties of the sintered specimens. Therefore, it becomes imperative to develop an appropriate heating process utilizing the MW technology in order to minimize defects.

3.1.2. Effect of processing conditions on mechanical properties

The effect of dwell time on the mechanical properties of the sintered ceramic cube specimens was evaluated. The stress-strain relations of the specimens under uniaxial compression are presented in Figure 5a, while the compressive strength and the Young's modulus of the specimens are summarized in Figure 5b and c, respectively. The mechanical properties of the sintered specimens showed an increasing trend with longer dwell times. Specimens fabricated through the SMWH process exhibited better mechanical properties compared to those prepared through conventional furnace heating. At a dwell time of 10 min, the compressive strength of MW10m was measured to be 34.92 ± 3.49 MPa, which is 80% higher than that of the CS180m. The compressive strength sharply increased to 86.62 ± 8.2 MPa for MW120m. As the dwell time was further increased, the enhancement in compressive strength became less pronounced, reaching a peak of 101.35 ± 19.62 MPa for the MW180m specimens. In comparison, the specimens prepared using a conventional furnace exhibited much lower compressive strength values at each dwell time, indicating significant enhancement of mechanical properties through the SMWH process.

The Young's modulus of the specimens prepared through the SMWH process shows a similar trend with compressive strength with longer dwell times, which were also notably higher compared to the specimens prepared through the conventional furnace heating. At a dwell time of 10 min, the MW10m exhibited a modulus of 1.94 ± 0.02 GPa, which gradually increased to 2.79 ± 0.17 GPa for MW180. In contrast, the modulus values of the specimens prepared through the conventional heating process were over 50% lower at each dwell time, ranging from 0.87 ± 0.07 to 1.07 ± 0.14 GPa. The significant improvement in mechanical properties observed in the ceramic cube specimens is primarily attributed to the accelerated densification process facilitated by the SMWH process. In addition, the increased formation of cristobalite phase further contributes to the enhancement of mechanical strength.²⁶ The specimens prepared through conventional heating exhibit lower relative density, and therefore lower mechanical strength was recorded. The SMWH process offers several advantages including rapid and more homogenous heating. This is achieved through a unique two-way heating mechanism that combines the conventional mode of heating transfer from the MW susceptor with the direct interaction between the MW field and the target materials.³² While prolonged sintering time can improve the mechanical properties of the specimens, it was found when the dwell time further increased from 120 to 180 min, the improvement in the mechanical properties is limited. Consequently, a 120-min dwell time for the sintering stage of the ceramic specimens was chosen for the remaining of the study.

3.2. Susceptor-assisted hybrid pyrolysis-sintering process

To address defects caused by debinding and sintering and improve the quality of the sintered ceramic specimens, we developed an innovative SHPS process. Figure 6a illustrates the SHPS process for the DLP-printed specimens. During the first heating stage, instead of directly removing the binder in the 3D-printed structures in conventional process, a pyrolysis step at 600°C under N_2 atmosphere was introduced. Based on the TGA analysis, the majority of heteroatoms, including oxygen and hydrogen, were eliminated at this temperature. Consequently, the organic constituents underwent a transformation into pyrolytic carbon, resulting in substantial structural shrinkage. After pyrolysis, the SiO_2 particles were brought closely together before the complete removal of the residual pyrolytic carbon. This particle motion can improve the densification during sintering. After the pyrolysis step, the specimens were then subjected to a sintering step under air atmosphere. An intermediate heating step was introduced at 800°C for complete removal of the pyrolytic

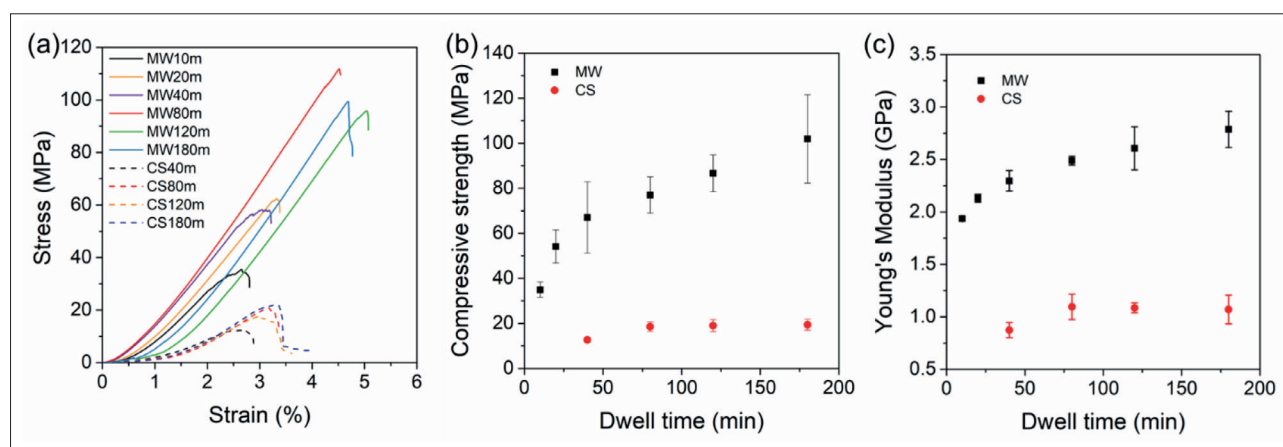


Figure 5. Stress–strain curves (a), compressive strength (b), and Young's modulus (c) of the 3D-printed ceramic cube specimens prepared through SMWH and conventional furnace heating.

carbon, followed by sintering at 1150°C. Throughout the sintering phase, the pyrolytic carbon potentially functions as a microwave susceptor, aiding in the heating process and enhancing heating uniformity.³³ Due to the reduced gas generation and closer particle packing during the sintering stage, fewer defect voids were formed. This suppression of void formation significantly reduces crack formation and improves densification. This is evidenced by the SEM observation of the SHPS120m specimens as shown in Figure 6b (the red arrow indicates the location of cracks). In order to compare the efficacy of SMWH process and the SHPS process, the 3D-printed cube structures were also subjected to the conventional heating following the manufacturer's recommendations (RCS120m). As shown in Figure 6c, abundant cracks can be observed for the sintered RCS120m specimens, regardless of the slow heating rate and cooling rate employed. Although the number of cracks was reduced compared to the MW120m specimens, it was still significantly higher compared to the SHPS120m specimens. The formation of cracks in RCS120m was attributed to the uneven heating resulting from the conventional heating mode. Moreover, the slow heating rate prolonged the generation and release of gases during the debinding process. These may lead to the generation of internal stress which promote the formation of defects including voids and cracks.³⁴ To support this claim, the 3D μ -CT images of the specimens were compared, as shown in Figure 6e. Although cracks still present in the SHPS120m specimen, the volume was significantly reduced compared to the RCS120m and MW120m specimens. Table 2 summarizes the defect volume ratio and the relative density of the SHPS120m, RCS120m, and MW120m specimens. The total defect volume ratio for SHPS120m specimen is reduced to 3.86%, a 16.81% reduction compared to the RCS120m

specimen with a defect volume ratio 4.64%. Moreover, SHPS120m specimen also exhibits the highest relative density of $98.36 \pm 0.54\%$ among the three specimens. These findings provide evidence for higher quality of the sintered specimens achieved through the SHPS process.

The crystalline phases of the specimens were also investigated through XRD analysis, as presented in Figure 7a. Both SHPS120m and MW120m show similar XRD patterns, with predominate peaks corresponding to the cristobalite phase at 21.8° and 36.1°. This suggests that the influence of the different heating profile of under MW heating process is minimal compared to dwell time. In contrast, RCS120m exhibits a weak peak intensity only at 21.8°, accompanied by a broad peak at 21.3°. This indicates that the transformation of SiO_2 from amorphous phase to the cristobalite phase is limited, regardless of the long processing time under the manufacturer's recommended heating profile.

Figure 7b depicts the comparison between compressive stress–strain curves of the SHPS120m, RCS120m, MW120m, and CS120m specimens. Compared to CS120m specimen, with a higher heating rate, the relative density and compressive strength of RCS120m improved by 1.64% and 91.72%, respectively. Furthermore, the defect volume of RCS120m reduced significantly from 16.13% to 4.64%. This is mainly attributed to the gradual heating rate at temperatures below 600°C. This slower heating facilitates the slower generation and release of pyrolysis gases, allowing for complete binder decomposition during the debinding process. On the other hand, the SHPS120m specimens show significant improvements in mechanical properties. Specifically, they exhibited a compressive strength of 158.35 ± 19.76 MPa and a modulus of 3.14 ± 0.04 GPa. These values represent roughly 83% and 20%

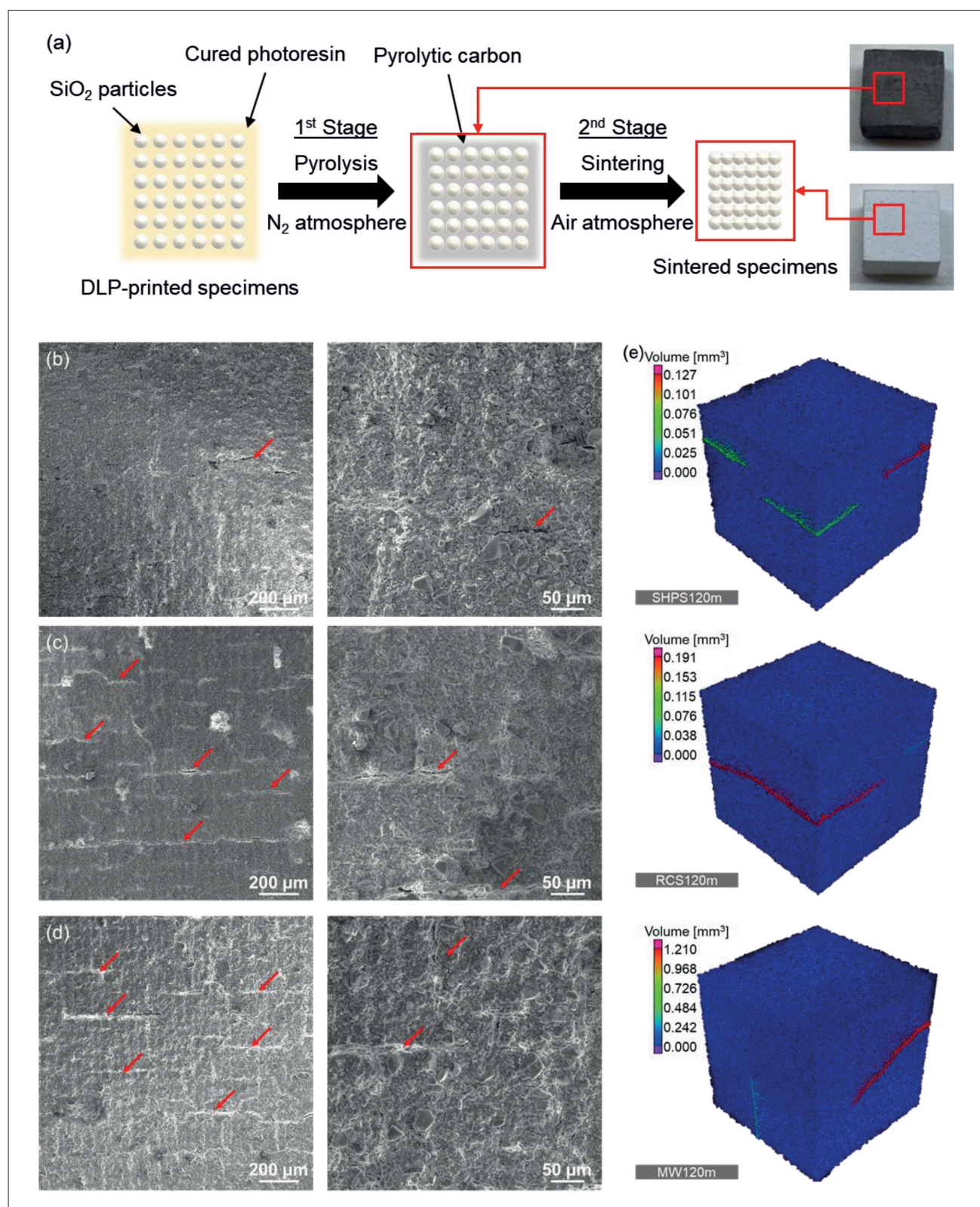


Figure 6. Morphological analysis of specimens fabricated through different processes. (a) Illustration of the pyrolysis and sintering of 3D-printed specimen using susceptor-assisted hybrid pyrolysis-sintering (SHPS) process. The scanning electron microscopic (SEM) images for sintered (b) SHPS120m, (c) RCS120m, (d) MW120m specimens, and (e) the corresponding reconstructed micro-computed tomography (μ -CT) 3D image for defect identification.

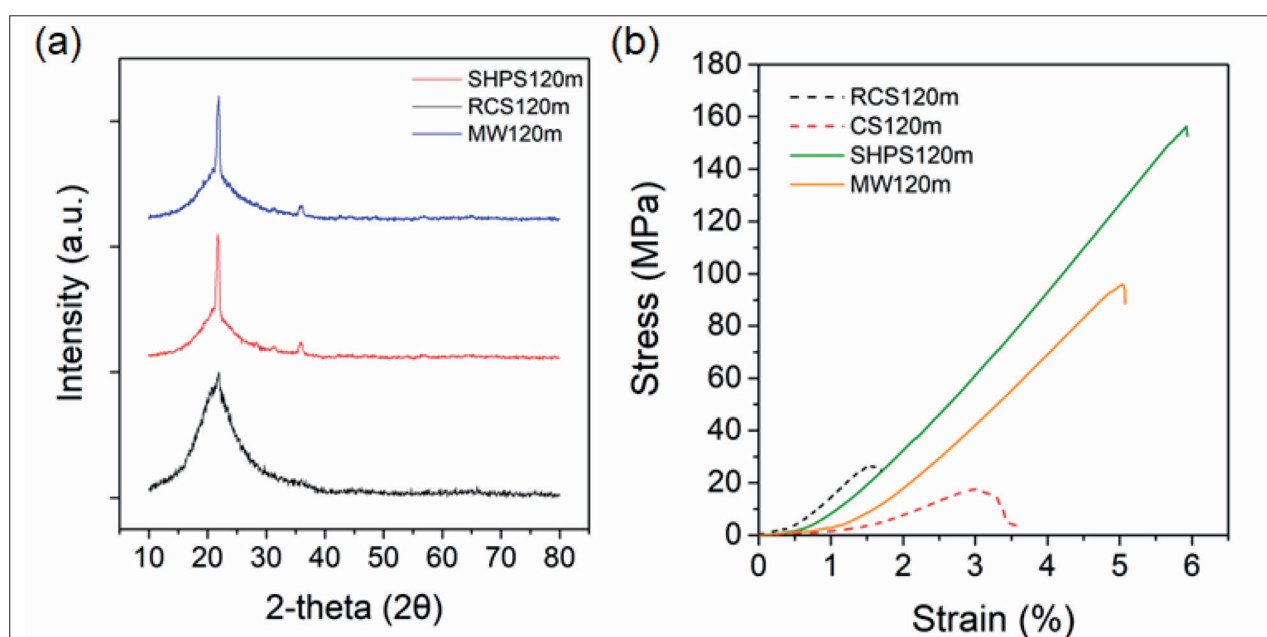


Figure 7. Comparative analysis of specimens fabricated using different processes. (a) X-ray diffraction (XRD) pattern for SHPS120m, RCS120m, and MW120m. (b) The stress–strain curve of the ceramic cube specimens prepared through different heating profiles.

increase, respectively, compared to MW120m. Additionally, compared to RCS120m, SHPS120m specimens showed a remarkable 336% increase in compressive strength and a 28% increase in Young's modulus. The SHPS process leads to a much denser specimen with minimized defects, thereby significantly enhancing the mechanical properties. Therefore, this process was employed for the post-thermal treatment of DLP-printed sheet gyroid structures to ensure the quality of the 3D ceramic scaffold. The compressive strength and Young's modulus of the specimens are summarized in Table 2.

3.3. Characterization of DLP-printed gyroid scaffold

Figure 8a shows the SEM images of the sheet gyroid structures before and after the SHPS process, with different value of ϕ . The lamellar facets were examined to identify any structure defects. The DLP-printed sample displayed

a rough surface morphology, which is primarily due to the staircase artefacts formed from pixelated light and layer-by-layer forming mechanism of the DLP technology.³⁵ As observed, the pixelated morphology became more pronounced after sintering, but no signs of cracks, voids, and delamination of layers were observed. This suggests that the gyroid structures were successfully sintered, resulting in a dense specimen through the proposed SHPS method. The wall thickness and the pore diameter of the sheet gyroid structures were also investigated using ImageJ, and the results are summarized in Table 3. As ϕ increased, the wall thickness increases, measuring at 274.1 ± 15.5 , 374.6 ± 15.1 , and 475.7 ± 25.5 μm for 40VF-gy, 50VF-gy, and 60VF-gy, respectively. Conversely, the pore diameters decreased as the ϕ increased, with values of 674.3 ± 24.9 , 576.8 ± 15.0 , and 528.4 ± 28.6 μm for 40VF-gy, 50VF-gy, and 60VF-gy, respectively.

Table 2. Summary of the physical properties, including the defect volume ratio, relative density, compressive strength, elastic modulus, and hardness of the sintered SHPS120m, RCS120m specimens, and MW120m.

Sintered sample	Defect volume ratio (%)	Relative density (%)	Compressive strength (MPa)	Young's modulus (GPa)
SHPS120m	3.86	98.36 ± 0.54	158.35 ± 19.76	3.14 ± 0.04
MW120m	7.22	96.95 ± 0.48	86.62 ± 8.2	2.61 ± 0.21
RCS120m	4.64	95.02 ± 0.61	36.35 ± 0.26	2.45 ± 0.07
CS120m	16.13	93.49 ± 0.35	18.96 ± 2.66	1.08 ± 0.05

Figure 8b presents the surface deviation maps of the DLP-printed gyroid structures (before sintering) compared with the CAD models from the 3D μ -CT analysis. As observed, the surface deviation of all specimens laid within -250 to 250 μm . The major reason for the deviation is attributed to the accuracy of the DLP printer, which is defined by the pixel size (i.e., resolution) of the machine. The porosity of the DLP-printed structures was also evaluated through μ -CT analysis and compared with the designed model. The porosity of 40VF-gy, 50VF-gy, and 60VF-gy after SHPS process were recorded as 57.30%, 46.36%, and 41.64%, respectively. A maximum deviation of 7.28% was obtained, suggesting a close matching with the designed model.

3.4. Mechanical properties of the gyroid with and without structural isotropy

In Figure 9a and b, the compressive properties of the sheet gyroid with different value of ϕ are compared. The compressive strength and the Young's modulus of the gyroid structure follow the trend of ϕ . The 60VF-gy exhibited better mechanical properties with a compressive strength of 15.62 ± 1.94 MPa and a modulus of 2.09 ± 0.29

GPa, which was reduced by 90.1% and 33.4%, respectively, compared to the SHPS120m specimens. In contrast, the mechanical strength of the 40VF-gy reduced, with a compressive strength of 6.51 ± 0.40 MPa and a modulus of 1.07 ± 0.05 GPa. This is primarily due to the higher porosity of the specimens.

To investigate the effect of the lattice structure designs of the gyroid structure on the mechanical properties, compressive tests were conducted in both normal (N) and transverse (T) directions. Cubic gyroid structures having radial graded porosity and approximately the same porosity (i.e., $\phi = 57.55\%$) were generated using unit cells with aspect ratios of 1 (γ .50-FGgy), 1.5 (γ .33-FGgy), and 2 (γ .25-FGgy). Figure 9c depicts the compressive strength of 57.55VF-gy, γ .25-FGgy, γ .33-FGgy, and γ .50-FGgy, respectively. The compressive strength of the 57.55VF-gy was recorded as 13.97 ± 2.20 MPa. It was observed that, despite having similar porosity, the anisotropic mechanical properties were achieved for γ .25-FGgy, γ .33-FGgy, and γ .50-FGgy specimens. In the transverse direction, γ .25-FGgy showed over a threefold increase in compressive strength compared to 57.55VF-gy, with a value of 44.51 ± 3.32 MPa. The aspect

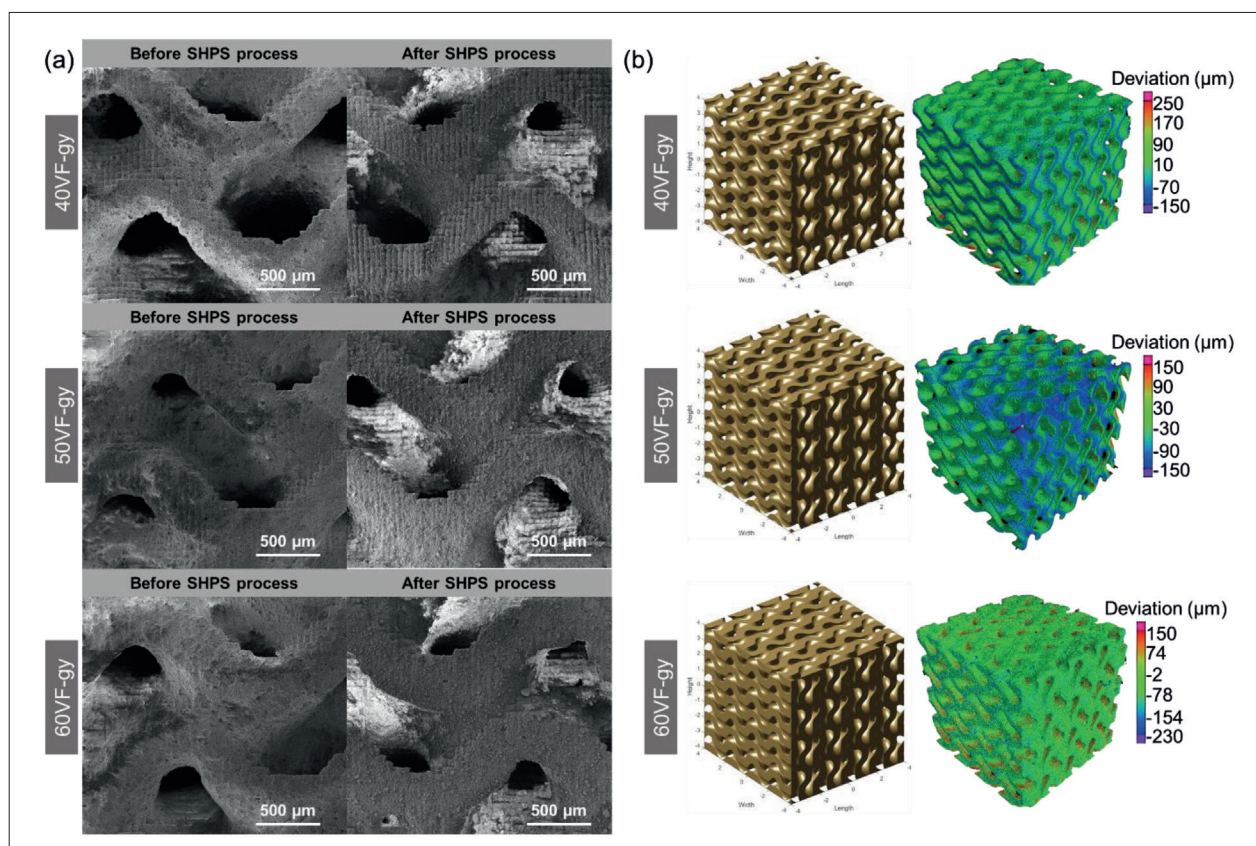


Figure 8. Characterization of SiO_2 gyroid scaffolds. (a) The corresponding scanning electron microscopic (SEM) images before and after the SHPS process. (b) 3D Surface deviation map of the digital light processing (DLP)-printed gyroid structures with different volume fractions ($\neq \phi$).

Table 3. Summary of the physical properties of the DLP-printed structures and the sintered specimens.

Sample	DLP-printed structures			Sintered specimens	
	Designed porosity (%)	Porosity after sintering (%)	Deviation (%)	Wall thickness (μm)	Pore diameter (μm)
40VF-gy	60	57.30	4.50%	274.1 ± 15.5	674.3 ± 24.9
50VF-gy	50	46.36	7.28%	374.6 ± 15.1	576.8 ± 15.0
60VF-gy	40	41.64	4.10%	475.7 ± 25.5	528.4 ± 28.6

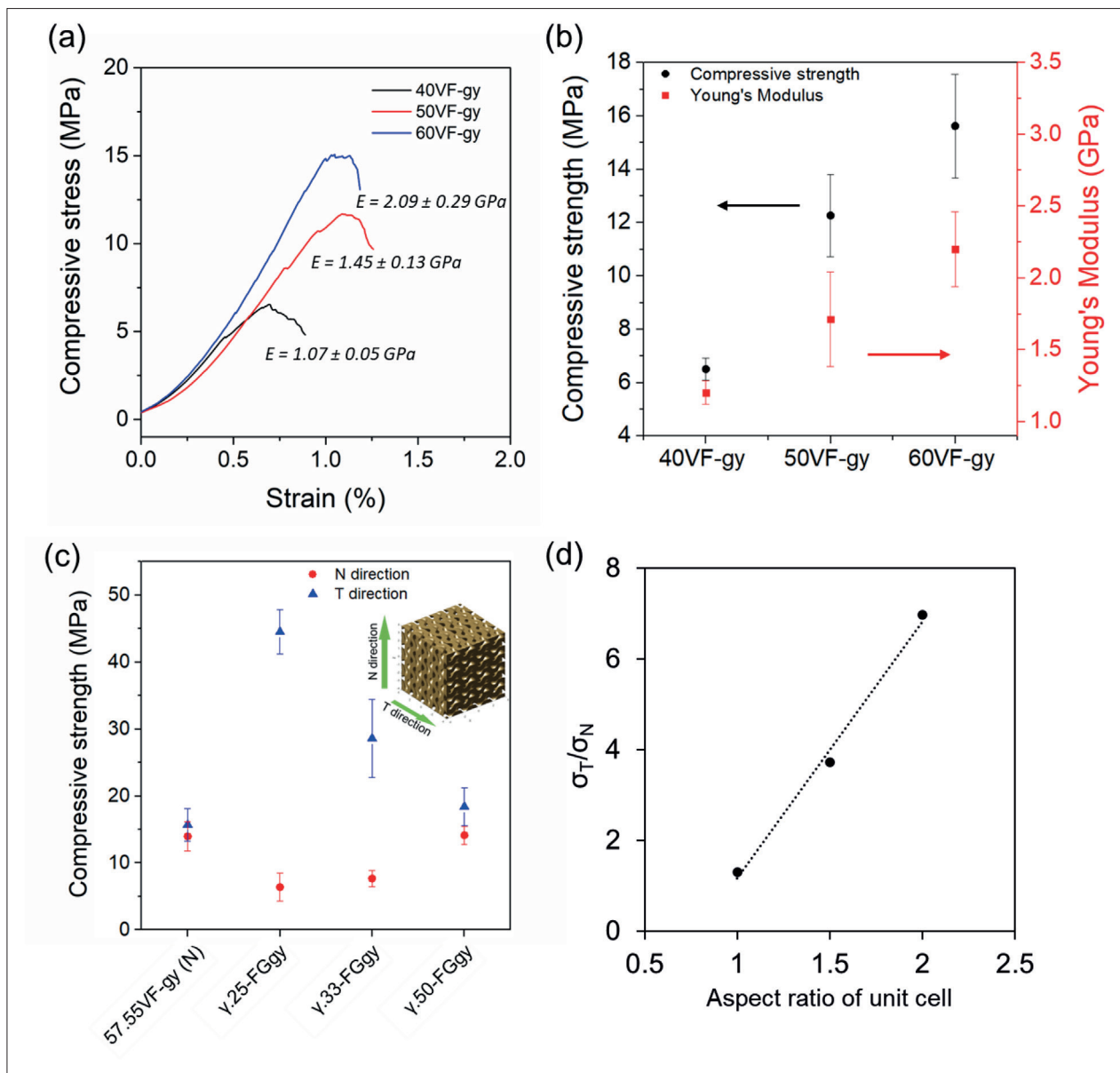


Figure 9. Mechanical properties of SiO₂ gyroid scaffolds with anisotropic properties. (a) The stress–strain curve, (b) compressive strength and Young's modulus of 40VF-gy, 50VF-gy, and 60VF-gy. (c) Compressive strength of 57.55VF-gy, γ .25-FGgy, γ .33-FGgy, and γ .50-FGgy (the compression tests of graded gyroid structures were performed in normal [N] direction and the transverse [T] direction), and (d) the relation between the ratios of the compressive strength in the T direction and the N direction (i.e., σ_T/σ_N) and the aspect ratio of the unit cell.

ratio of the unit cell and the compressive strength of the graded gyroid structure demonstrated a proportional relationship in the transverse direction. The compressive strengths of γ .33-FGgy and γ .50-FGgy were recorded as 28.59 ± 5.83 and 18.40 ± 2.78 MPa, respectively. In contrast, as the aspect ratio decreased from 2 to 1, the compressive strength in the normal direction showed an increasing trend, rising from 6.38 ± 2.08 to 14.14 ± 1.38 MPa. The anisotropic properties of the specimens can be compared using the ratios of the compressive strength in the transverse direction and the normal direction (i.e., σ_T / σ_N). The ratio σ_T / σ_N for γ .25-FGgy, γ .33-FGgy, and γ .50-FGgy are 6.97, 3.72, and 1.3, respectively. The results indicate that despite the pore distribution, the gyroid structure with a higher aspect ratio of the unit cell can result in higher degree of anisotropy (Figure 9d). These findings are particularly useful for bioscaffold design, strategy to mimic the anisotropic properties of native bone. This approach helps mitigate the stress shielding effect, thereby enhancing scaffold integration *in vivo*.

3.5. *In vitro* study

The cytocompatibility of the gyroid scaffolds was evaluated by seeding BMSCs directly onto various scaffold designs, including 57.55VF-gy, γ .50-FGgy, γ .33-FGgy, and γ .25-FGgy. To investigate the effect of the scaffolds' anisotropic properties, a fixed porosity of 57.55% and overall dimensions of $8 \times 8 \times 8$ mm³ were selected. Cell viability and proliferation were assessed at 1, 3, and 7 days of culture. Confocal microscope images, as shown in Figure 10a, revealed an even distribution of cells on the scaffolds after 3 days. According to the live/dead cell viability assay (Figure 10b), all scaffold groups exhibited over 98% cell viability, indicating excellent cytocompatibility. The effects of the scaffold structures of the scaffolds were further evaluated by investigating cell seeding efficiency over different time points. The surface area of each scaffold model, presented in Figure 10b, shows that all scaffolds supported cell proliferation over the culture period, albeit with varying efficiencies (Figure 10c). Among the different specimens, the γ .50-FGgy scaffold demonstrated better cell

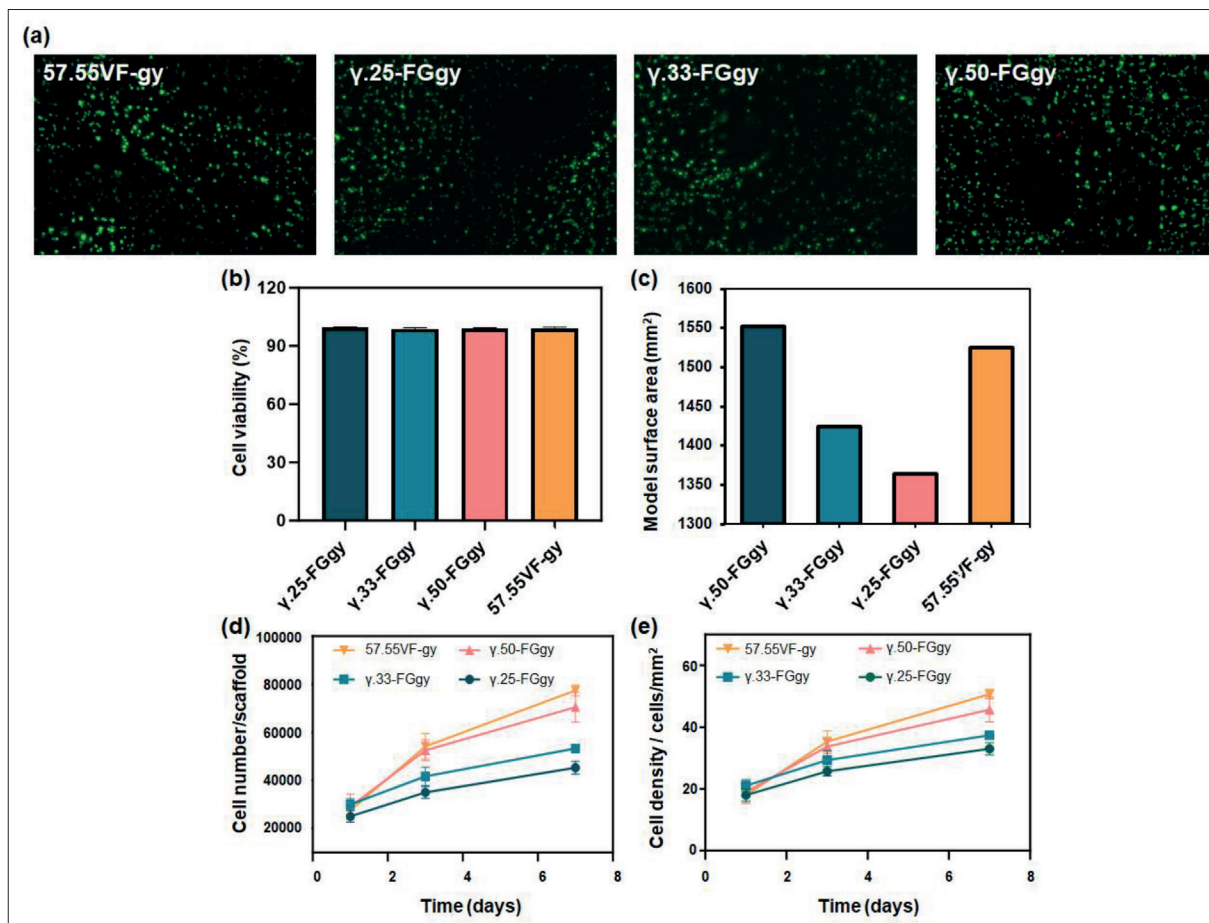


Figure 10. Live/dead staining (a), cell viability (b), models surface area (c) of the scaffolds, as well as cell number (d) and cell density (e) of the gyroid scaffolds.

proliferation efficiency, with a higher cell count observed at day 7. Conversely, the γ .25-FGgy scaffold exhibited the slowest cell proliferation rate. This decrease in proliferation rate correlates with the reduction in total surface area, which decreases from 1551.9 mm² for γ .50-FGgy to 1363.8 mm² for γ .25-FGgy. Additionally, as the aspect ratio of the unit cell of the gyroid structures increases with lower γ values, the average Gaussian curvatures of the scaffolds are affected. This alteration in curvature can significantly impact the proliferation behavior of mesenchymal stem cells, as supported by previous studies.^{7,36} To further evaluate the cell seeding efficiency, the cell density on the scaffold over the 7-day culture period was calculated by normalizing the cell number to the surface area (Figure 10d). As the γ value decreased (indicating a higher aspect ratio), the cell counts per square millimeter of scaffold surface area decreased significantly, from 46 cells/mm² for γ .50-FGgy to 33 cells/mm² for γ .25-FGgy. This finding suggests that while anisotropic properties of the scaffold can be achieved by tuning the γ value, there is a trade-off in cell proliferation rates. In comparison, the 57.55VF-gy specimens, which lacked porosity gradients, exhibited the highest cell density after 7 days of culture. This indicates that the presence of structural gradients, while beneficial for mimicking natural bone anisotropy, may reduce the overall cell proliferation rate due to the decreased effective surface area and altered curvature. Overall, these results indicate that gyroid scaffolds with anisotropic properties offer notable benefits in mimicking natural bone structures and could potentially mitigate *in vivo* stress shielding. In addition, designing them requires careful consideration to strike a balance between mechanical properties and optimal cell proliferation rates.

4. Discussion

This study introduces a mathematical design approach for customizing 3D bioscaffolds. By setting appropriate geometric parameters (α , β , and γ) and the iso-surface function $C(x, y, z)$ in the level-set equations, sheet gyroid scaffolds with spatially controlled porosity and anisotropic properties were generated. Given that other types of TPMS share similar mathematical descriptions, this design approach does not limit to sheet gyroid structures but can also be applied to other TPMS variations. Moreover, we established an innovative SHPS processing method, utilizing MW heating technology, to effectively debind and sinter the 3D-printed ceramic green specimens. The comparison between SMWH process and conventional furnace heating highlights the advantages of MW technology in ceramic processing. Additionally, the SHPS process addresses the critical challenge associated with MW technology in

sintering 3D-printed ceramic structures, such as crack formation, thus offering a promising solution to enhance the quality of 3D-printed ceramic scaffold. By integrating advanced functional materials like piezoelectric ceramics, this processing method will accelerate the development of 3D-printed ceramic structures for cutting-edge biodevices.

The comparative study between SMWH process and conventional furnace heating revealed advantages of MW technology in enhancing the physical and mechanical properties of the ceramic specimens. The compressive strength of the MW120m was measured at 86.62 ± 8.2 MPa, over 1.8 times higher than the compressive strength of RCS120m. The SMWH process resulted in higher relative densities and different crystalline structures compared to conventional furnace heating, which contributed to the mechanical enhancement of the 3D-printed specimens. The SMWH process facilitates rapid and efficient energy transfer to 3D-printed ceramic specimens through a two-way heating mechanism.^{23,32} This rapid energy transfer of MW heating decreases sintering activation energy and processing temperature,^{19,20} promoting densification,³⁷ which result in an improvement in relative density from 95.02% to 96.95%. Additionally, the intrinsic heating mechanism of MW technology reduces activation energy for nucleation and enhances crystallization during the sintering process.²⁰ Despite the significant enhancements in the mechanical properties, severe crack formation was observed, indicating the need for further improvement of the SMWH process.

An innovative SHPS process was established to reduce the defects caused by debinding and sintering. From the morphological and physical characterizations, the process led to denser ceramic specimens after sintering with minimized defects compared to both SMWH and conventional furnace heating. SEM and μ -CT analyses (Figure 6) confirmed the reduction in crack formation and defect volume in SHPS specimens. Compared with RCS120m which had a defect volume of 4.64%, the defect volume of SHPS120m was reduced by 16.80–3.86%. Consequently, a significant improvement in mechanical properties for SHPS120m specimens was recorded, with about 335% increase in compressive strength (158.35 ± 19.76 MPa) and a 28.2% in Young's modulus (3.14 ± 0.04 GPa), respectively.

The reduction of defects is primarily attributed to the additional pyrolysis step during the SHPS process. Unlike traditional debinding methods that involve removing the polymer, the polymer is transformed into carbon during pyrolysis. Pyrolysis transforms the polymer into carbon. This transformation potentially reduces gas formation and release during the process,

while particle motion occurs as the structure shrinks during pyrolysis. As a result, the SiO_2 particles become tightly packed, thereby enhancing densification during subsequent sintering steps. This improvement leads to enhanced relative density and mechanical properties. These results highlight the promising potential of SHPS method as a post-processing technique for enhancing the quality of 3D-printed ceramic structures. Additionally, it is anticipated that the formulating photosensitive slurry with advanced functional materials such as piezoelectric ceramics can further enhance the potential of the SHPS method. Piezoelectric ceramics possess unique properties that enable them to convert mechanical energy into electrical energy and vice versa. By integrating piezoelectric ceramics into 3D-printed ceramic structures, it becomes possible to develop biodevices with advanced functionalities, such as sensors and actuators.³⁸

To demonstrate the practical application of the SHPS method, gyroid scaffolds with different geometries were fabricated. The morphology and mechanical properties of the specimens were investigated. SEM images revealed the pixelated morphology of specimens after sintering, and no cracks, voids, or delamination were observed. The gyroid structures exhibited varying mechanical strengths and porosities depending on their design parameters, such as volume fraction and lattice structure. Results showed that compressive strength and Young's modulus followed the trend of ϕ . As the volume fraction increases, the mechanical properties also increase, with the highest compressive strength of 15.62 ± 1.94 MPa and a modulus of 2.09 ± 0.29 GPa for 60VF-gy. Additionally, the effects of the aspect ratio of the unit cell on the mechanical properties of gyroid structures were investigated. Gyroid scaffolds with anisotropic mechanical properties were fabricated despite having a radially graded porosity distribution. The aspect ratio of the unit cell structure affects the compressive strength of the scaffolds in the normal (σ_N) and transverse directions (σ_T). As the aspect ratio increased from 1 to 2, the ratio of σ_T to σ_N increases from 1.3 to 6.97, indicating a higher degree of anisotropy. The proposed mathematical design approach offers an effective strategy for manipulating the anisotropic properties of ceramic scaffolds, thus possessing great potential to mitigate the stress shielding effect under *in vivo* conditions and promoting bone regeneration.⁸ These findings can contribute to the development of ceramic scaffolds with tailorable mechanical properties, offering promising prospects for advancing bone tissue engineering and regeneration applications.

In vitro cell studies were conducted to evaluate the cytocompatibility of gyroid scaffolds with radially graded structures. Confocal microscope images revealed even cell

distribution on all scaffolds, with over 98% cell viability observed across all sample groups, indicating excellent biocompatibility. The gyroid structures demonstrated varying cell proliferation efficiencies, which can be attributed to differences in total surface area and Gaussian curvatures. Specifically, gyroid structures with higher γ values (indicating a lower aspect ratio of the unit cell) exhibited higher surface areas (as shown in Table 1 and Figure 10c), which correlated with higher cell counts. For example, the $\gamma_{.50}$ -FGgy scaffold showed superior cell proliferation efficiency, with significantly higher cell counts observed on day 7. In contrast, the $\gamma_{.25}$ -FGgy scaffold exhibited a slight decrease in cell proliferation rate. This variation in cell proliferation rates provides valuable insight into how the geometric features of graded gyroid structures affect regenerative performance. The findings suggest that increasing the surface area by adjusting the γ value can enhance cell attachment and proliferation, likely due to the increased hyperboloidal surfaces for cell adhesion and retention. Overall, this work presents a promising strategy for efficiently producing high-quality ceramic scaffolds with customizable geometries that can be tailored to specific biological needs. The ability to fine-tune the geometric parameters of gyroid structures offers significant potential for optimizing scaffold design for various bone regeneration scenarios. However, additional investigation is suggested to further refine these designs and to optimize the gyroid structures for specific *in vivo* bone regeneration applications. Future studies should focus on understanding the long-term effects of these geometric variations on bone healing and integration, as well as exploring the potential for combining these scaffolds with bioactive coatings or growth factors to enhance their regenerative capabilities.

5. Conclusion

This study has successfully demonstrated a computer-aided design approach for generating gyroid structures with tailored properties. By manipulating the geometrical parameters within the level-set equation of the gyroid structure, we are able to adjust the aspect ratio of the unit cell and fabricate structures with radially graded porosity that can mimic the architecture of trabecular bone. A rapid SMWH method was developed, hybridizing the pyrolysis and sintering process, which resulted in significant improvements in the structure quality. This process notably reduced the defect volume in the sintered ceramic structures by 16.81% and remarkably enhanced the compressive strength by 336% compared to conventional furnace heating methods. Furthermore, the relations between geometric features and both mechanical performance

and *in vitro* cellular responses were investigated. It was observed that an increase in the aspect ratio of the unit cell significantly amplified the anisotropic mechanical properties of the gyroid structure. However, this modification slightly reduced cell proliferation efficiency in comparison to the uniform gyroid structure, which can be attributed to variations in Gaussian curvatures. This study presented an effective design methodology for TPMS, including but not limited to gyroid structures, with tailored properties. Our methodology can be extended to the design of smart scaffolds incorporating piezoelectric materials for bone implants beyond traditional materials.

Acknowledgments

The authors gratefully acknowledge the support from U3DP of The Hong Kong Polytechnic University, and extend special thanks to Tab Cheng and Sidney Wong for their valuable assistance.

Funding

The work described in this paper was mainly supported by the funding support to the State Key Laboratories in Hong Kong from the Innovation and Technology Commission (ITC of the Government of the Hong Kong Special Administrative Region [HKSAR] of China), and The Hong Kong Polytechnic University (Project Code: BBX2 and PolyU Project Code: 1-BBTN) and a grant from the Research Committee of The Hong Kong Polytechnic University under project account code G-UAMY.

Conflict of interest

The authors declare they have no competing interests.

Author contributions

Conceptualization: Ka-Wai Yeung, Chak-Yin Tang

Data curation: Ka-Wai Yeung, Chi-Yeung Mang, Quan-Jing Mei

Funding acquisition: Chak-Yin Tang

Investigation: Ka-Wai Yeung, Quan-Jing Mei

Methodology: Ka-Wai Yeung, Chi-Yeung Mang

Supervision: Chak-Yin Tang

Visualization: Ka-Wai Yeung

Writing – original draft: Ka-Wai Yeung

Writing – review & editing: Chi Ho Wong, Chak-Yin Tang, Xin Zhao, Wing-Cheung Law, Gary Chi-Pong Tsui, Zhenjia Huang

Ethics approval and consent to participate

Not applicable.

Consent for publication

Not applicable.

Availability of data

Data is available from the corresponding author upon reasonable request.

References

1. Vijayavenkataraman S, Kuan LY, Lu WF. 3D-printed ceramic triply periodic minimal surface structures for design of functionally graded bone implants. *Mater Design*. 2020;191:108602. doi: 10.1016/j.matdes.2020.108602
2. Yan C, Hao L, Hussein A, Young P. Ti–6Al–4V triply periodic minimal surface structures for bone implants fabricated via selective laser melting. *J Mech Behav Biomed Mater*. 2015;51:61–73. doi: 10.1016/j.jmbbm.2015.06.024
3. Dong Z, Zhao X. Application of TPMS structure in bone regeneration. *Eng Regen*. 2021;2(8):154–162. doi: 10.1016/j.engreg.2021.09.004
4. Shan Y, Bai Y, Yang S, et al. 3D-printed strontium-incorporated β -TCP bioceramic triply periodic minimal surface scaffolds with simultaneous high porosity, enhanced strength, and excellent bioactivity. *J Adv Ceram*. 2023;12(9):1671–1684. doi: 10.26599/JAC.2023.9220787
5. Al-Ketan O, Abu Al-Rub RK. MSLattice: a free software for generating uniform and graded lattices based on triply periodic minimal surfaces. *Mater Des Process Commun*. 2021;3(6):e205. doi: 10.1002/mdp2.205
6. Ma S, Song K, Lan J, Ma L. Biological and mechanical property analysis for designed heterogeneous porous scaffolds based on the refined TPMS. *J Mech Behav Biomed Mater*. 2020;107:103727. doi: 10.1016/j.jmbbm.2020.103727
7. Yang Y, Xu T, Bei H-P, et al. Gaussian curvature-driven direction of cell fate toward osteogenesis with triply periodic minimal surface scaffolds. *Proc Natl Acad Sci U S A*. 2022;119(41):e2206684119. doi: 10.1073/pnas.2206684119
8. Deering J, Dowling KI, DiCecco L-A, McLean GD, Yu B, Grandfield K. Selective Voronoi tessellation as a method to design anisotropic and biomimetic implants. *J Mech Behav Biomed Mater*. 2021;116:104361. doi: 10.1016/j.jmbbm.2021.104361

9. Yao Y, Qin W, Xing B, Sha N, Jiao T, Zhao Z. High performance hydroxyapatite ceramics and a triply periodic minimum surface structure fabricated by digital light processing 3D printing. *J Adv Ceram.* 2021;10(1):39-48. doi: 10.1007/s40145-020-0415-4
10. Li G, Li Z, Min Y, Chen S, Han R, Zhao Z. 3D-printed piezoelectric scaffolds with shape memory polymer for bone regeneration. *Small.* 2023;19(40):e2302927. doi: 10.1002/sml.202302927
11. Chen A, Su J, Li Y, et al. 3D/4D printed bio-piezoelectric smart scaffolds for next-generation bone tissue engineering. *Int J Extrem Manuf.* 2023;5(3):032007. doi: 10.1088/2631-7990/acd88f
12. Zhou Q, Su X, Wu J, et al. Additive manufacturing of bioceramic implants for restoration bone engineering: technologies, advances, and future perspectives. *ACS Biomater Sci Eng.* 2023;9(3):1164-1189. doi: 10.1021/acsbomaterials.2c01164
13. Ravi M, Paramesh V, Kaviya S, Anuradha E, Solomon FP. 3D cell culture systems: advantages and applications. *J Cell Physiol.* 2015;230(1):16-26. doi: 10.1002/jcp.24683
14. Ma J, Qin C, Wu J, et al. 3D printing of strontium silicate microcylinder-containing multicellular biomaterial inks for vascularized skin regeneration. *Adv Healthc Mater.* 2021;10(16):e2100523. doi: 10.1002/adhm.202100523
15. Feng C, Zhang K, He R, et al. Additive manufacturing of hydroxyapatite bioceramic scaffolds: dispersion, digital light processing, sintering, mechanical properties, and biocompatibility. *J Adv Ceram.* 2020;9:360-373. doi: 10.1007/s40145-020-0375-8
16. Chen Z, Li Z, Li J, et al. 3D printing of ceramics: a review. *J Eur Ceram Soc.* 2019;39(4):661-687. doi: 10.1016/j.jeurceramsoc.2018.11.013
17. Ren X, Wang J, Wu Y, et al. One-pot synthesis of hydroxyapatite hybrid bioinks for digital light processing 3D printing in bone regeneration. *J Mater Sci Technol.* 2024;188:84-97. doi: 10.1016/j.jmst.2024.01.001
18. Li Y, Su J, Chen A, et al. Strontium-doped calcium silicate scaffolds with enhanced mechanical properties and tunable biodegradability fabricated by vat photopolymerization. *Int J Bioprint.* 2023;9(6):1233. doi: 10.36922/ijb.1233
19. Akinwekomi AD, Yeung K-W, Tang C-Y, Law W-C, Tsui GC-P. Finite element simulation of hybrid microwave sintering based on power approach. *Int J Adv Manuf Technol.* 2020;110:2503-2515. doi: 10.1007/s00170-020-05952-0
20. Zuo F, Badev A, Saunier S, Goeuriot D, Heuguet R, Marinel S. Microwave versus conventional sintering: estimate of the apparent activation energy for densification of α -alumina and zinc oxide. *J Eur Ceram Soc.* 2014;34(12):3103-3110. doi: 10.1016/j.jeurceramsoc.2014.04.006
21. Tang J, Xu J, Ye Z, Li X, Luo J. Microwave sintered porous CoCrFeNiMo high entropy alloy as an efficient electrocatalyst for alkaline oxygen evolution reaction. *J Mater Sci Technol.* 2021;79:171-177. doi: 10.1016/j.jmst.2020.10.079
22. Yeung K-W, Tang C-Y, Hu R, et al. Fabrication of ceramic bioscaffolds from fly ash cenosphere by susceptor-assisted microwave sintering. *J Eur Ceram Soc.* 2022;42(2):4410-4419. doi: 10.1016/j.jeurceramsoc.2022.03.046
23. Garnault T, Bouvard D, Chaix J-M, Marinel S, Harnois C. Is direct microwave heating well suited for sintering ceramics? *Ceram Int.* 2021;47(12):16716-16729. doi: 10.1016/j.ceramint.2021.02.242
24. Zhou M, Liu W, Wu H, et al. Preparation of a defect-free alumina cutting tool via additive manufacturing based on stereolithography–Optimization of the drying and debinding processes. *Ceram Int.* 2016;42(10):11598-11602. doi: 10.1016/j.ceramint.2016.04.050
25. Cui H, Hensleigh R, Yao D, et al. Three-dimensional printing of piezoelectric materials with designed anisotropy and directional response. *Nature Mater.* 2019;18(3):234-241. doi: 10.1038/s41563-018-0268-1
26. Zhanmanesh M, Varmazyar M, Montazerian H. Fluid permeability of graded porosity scaffolds architected with minimal surfaces. *ACS Biomater Sci Eng.* 2019;5(3):1228-1237. doi: 10.1021/acsbomaterials.8b01400
27. Song K, Wang Z, Lan J, Ma S. Porous structure design and mechanical behavior analysis based on TPMS for customized root analogue implant. *J Mech Behav Biomed Mater.* 2021;115:104222. doi: 10.1016/j.jmbbm.2020.104222
28. Yeung K-W, Huang Z, Mang C-Y, et al. Fabrication of pre-designed 3D carbon based microstructures via two-photon vat photopolymerization and susceptor-assisted microwave post-processing. *Addit Manuf.* 2023;79(16):103934. doi: 10.1016/j.addma.2023.103934
29. Arita R, Iijima M, Fujishiro Y, et al. Rapid three-dimensional structuring of transparent SiO₂ glass using interparticle photo-cross-linkable suspensions. *Commun Mater.* 2020;1(1):30. doi: 10.1038/s43246-020-0029-y
30. Zhao D, Su H, Hu K, et al. Formation mechanism and controlling strategy of lamellar structure in 3D printed alumina ceramics by digital light processing. *Addit Manuf.* 2022;52:102650. doi: 10.1016/j.addma.2022.102650

31. Wan W, Huang C-e, Yang J, Zeng J, Qiu T. Effect of sintering temperature on the properties of fused silica ceramics prepared by gelcasting. *J Electron Mater.* 2014;43(7):2566-2572. doi: 10.1007/s11664-014-3112-7
32. Yeung K-W, Chen L, Tang C-Y, et al. Rapid hybrid microwave cladding of SiO₂/TiO₂ sol-gel derived composite coatings. *J Sol-Gel Sci Technol.* 2021;98(1):35-44. doi: 10.1007/s10971-021-05498-x
33. Bhattacharya M, Basak T. A review on the susceptor assisted microwave processing of materials. *Energy.* 2016;97:306-338. doi: 10.1016/j.energy.2015.11.034
34. Liu Z, Ma C, Chang Z, Yan P, Li F. Advances in crack formation mechanism and inhibition strategy for ceramic additive manufacturing. *J Eur Ceram Soc.* 2023;43(12): 5078-5098. doi: 10.1016/j.jeurceramsoc.2023.05.008
35. Luongo A, Falster V, Doest MB, et al. Microstructure control in 3D printing with digital light processing. *Comp Graph Forum.* 2020;39(1):347-359. doi: 10.1111/cgf.13807
36. Schamberger B, Ziege R, Anselme K, et al. Curvature in biological systems: its quantification, emergence, and implications across the scales. *Adv Mater.* 2023;35(13):2206110. doi: 10.1002/adma.202206110
37. Karayannis VG. Microwave sintering of ceramic materials. *IOP Conf Ser Mater Sci Eng.* 2016;161(1):012068. doi: 10.1088/1757-899X/161/1/012068
38. Chorsi MT, Curry EJ, Chorsi HT, et al. Piezoelectric biomaterials for sensors and actuators. *Adv Mater.* 2019;31(1):e1802084. doi: 10.1002/adma.201802084